

Submitted to *Ap. J. Letters*; astro-ph/9604155

A Detection of Bright Features in the Microwave Background

M. S. Kowitt^{1,2}, E. S. Cheng¹, D. A. Cottingham³, D. J. Fixsen⁴, C. A. Inman^{2,1},
S. S. Meyer², L. A. Page⁵, J. L. Puchalla^{2,1}, J. E. Ruhl^{2,6}, and R. F. Silverberg¹

ABSTRACT

We report the characterization of bright, compact features in the cosmic microwave background radiation (CMBR) detected during the June 1992 and June 1994 balloon flights of the Medium Scale Anisotropy Measurement (MSAM1-92 and MSAM1-94, respectively). Spectral flux densities are determined for each feature at 5.7, 9.3, and 16.5 cm⁻¹. No viable counterparts for these features were found in source catalogs at 5 GHz or at 100 μ m. The measured spectrum of each feature is consistent with a temperature fluctuation in the CMBR. The existence of these features is consistent with adiabatic fluctuation models of anisotropy in the CMBR.

Subject headings: cosmic microwave background — cosmology: observations

1. Introduction

Recent observations of the cosmic microwave background radiation (CMBR) have found statistically significant anisotropy at 0°5 angular scales (see White, Scott, and Silk

¹Laboratory for Astronomy and Solar Physics, NASA/Goddard Space Flight Center, Code 685.0, Greenbelt, MD 20771

²Enrico Fermi Institute, University of Chicago, 5640 South Ellis Avenue, Chicago, IL 60637

³Global Science and Technology, Inc., Laboratory for Astronomy and Solar Physics, NASA/GSFC Code 685.0, Greenbelt, MD 20771

⁴Applied Research Corporation, Laboratory for Astronomy and Solar Physics, NASA/GSFC Code 685.3, Greenbelt, MD 20771

⁵Department of Physics, Princeton University, Princeton, NJ 08544

⁶Department of Physics, University of California, Santa Barbara, CA 93106

1994, and references therein). In earlier Letters (Cheng *et al.* 1994, hereafter Paper I, and Cheng *et al.* 1996, hereafter Paper II), we reported on observations of CMBR anisotropy that included two particularly bright features. The presence of bright, unresolved sources suggested the possibility of foreground point-source contamination, or of non-Gaussian fluctuations in the CMBR. In this Letter, we present our analysis of these features and a discussion of other work studying their properties.

2. Instrument and Observations

The MSAM1 instrument has been described in detail elsewhere (Fixsen *et al.* 1996); only the most relevant features are given here. MSAM1 is a balloon-borne off-axis Cassegrain telescope with a nutating secondary mirror and a four-band bolometric radiometer. The detectors have center frequencies of 5.7, 9.3, 16.5, and 22.6 cm^{-1} each with $\sim 1.5\text{ cm}^{-1}$ bandwidth. The beam size of the telescope is $28'$ FWHM, roughly independent of frequency. The secondary executes a horizontal four-position square-wave chop (i.e., center, left, center, right) with an amplitude of $\pm 40'$ on the sky. The telescope is pointed using a combination of torque motors and reaction wheels, referenced to a gyroscope. The absolute sky location is determined by star camera observation.

The data discussed here were collected during two flights of the MSAM instrument from Palestine, Texas; the first on 1992 June 5 (MSAM1-92), the second on 1994 June 2 (MSAM1-94). These observations have been described in Papers I and II, and are only summarized here. In each flight, the antenna patterns for all four bands were measured by rastering over Jupiter. We determine the location of the antenna pattern within the star camera's field-of-view to within $2'$ (post-flight) by simultaneously observing Jupiter in the star camera and the main telescope. Gyroscope drift increases our absolute pointing uncertainty to $\pm 2.5'$. We calibrate our spectral flux density measurements using the measured surface temperatures (Griffin *et al.* 1986) together with Jupiter's apparent diameter at the epoch of flight (Hagen and Boksenberg 1991, Donat III and Boksenberg 1993). The calibration has a 10% overall uncertainty, with relative errors of 1–4% between bands.

The CMBR observations were made at roughly constant declination $\delta \approx 82^\circ$, with the central beam covering right ascensions $14^{\text{h}}4$ – $16^{\text{h}}9$ and $17^{\text{h}}2$ – $20^{\text{h}}3$ during the MSAM1-92 flight. This corresponds to ~ 6.6 square degrees of sky coverage. The goal of the MSAM1-94 flight was to observe the identical field as MSAM1-92; this was nearly achieved, with an average declination difference of $\sim 10'$. The coverage in right ascension was somewhat less, extending from $15^{\text{h}}0$ – $17^{\text{h}}0$, and $17^{\text{h}}3$ – $20^{\text{h}}0$.

Except for §5, all results reported in this Letter are based on the MSAM1-92 observations.

3. Data Analysis

The initial data reduction used in this analysis has been reported in Papers I and II; only the salient features are reviewed here. Note that this Letter is based on the reanalyzed version of the MSAM1-92 data including the full instrument covariance matrix (Inman *et al.* 1996). Two nearly statistically independent demodulations are formed from the data. The single-difference demodulation subtracts the right beam from the left beam, and ignores the central beam data; the double-difference demodulation subtracts the average of the left+right beams from the central beam. The single-difference demodulation has an antisymmetric two-lobe response pattern, while the double-difference demodulation has a symmetric three-lobe pattern. The data are binned by position and angular orientation of the demodulated antenna pattern on the sky. To remove instrumental drift, a slowly varying function of time is fit simultaneously with the bins. The bin size is $0^\circ.12$ in position, and 10° in angular orientation.

The dominant sources of brightness contrast expected in our bands are anisotropy in the CMBR, and thermal emission from warm ($\sim 20\text{K}$) interstellar dust (Weiss 1980, Bennett *et al.* 1992). Before searching for compact features, we use one of our spectral degrees of freedom to make a simple correction for the presence of dust emission. Unlike our previous analyses for CMBR anisotropy, here we do not impose a full spectral model on the data. Rather, after a minimal correction for dust contamination, we model the spatial structure of several bright, compact features, and study the spectral nature of those features.

3.1. Foreground Dust Subtraction

We estimate and subtract the contribution of foreground interstellar dust emission using the 22.6 cm^{-1} band, assuming a $\nu^{1.5}$ emissivity Rayleigh-Jeans spectrum (the noise estimates in the remaining three bands are adjusted to reflect this subtraction). In making this correction, we assume that the 22.6 cm^{-1} band is an uncontaminated monitor of dust. Varying the exponent of the power law emissivity of the dust by ± 0.2 has a negligible effect on the final results, compared with the statistical uncertainties. The dust correction is most important for the 16.5 cm^{-1} band, and has little effect at the lower frequencies.

3.2. Search for Unresolved Features

After removing the estimated dust contamination, we search the remaining 3 frequency bands for unresolved features using an F –statistic to measure significance. Each band is searched independently, and then the source lists are compared. Since the telescope is scanned at roughly constant declination, we parameterize the location of the features as a function only of right ascension, and constrain the central declination of the feature to follow a slow linear function of right ascension.

We begin by calculating the raw χ^2 of the data in each band,

$$\chi_0^2 = \sum_{ij} (t_i - O_i) V_{ij}^{-1} (t_j - O_j),$$

where t_i are the binned data with associated noise covariance V_{ij} , and the sum is over both demodulations as well as bins. O_i is one of four arbitrary offset parameters corresponding to the two demodulations and two portions of the flight, appropriate to datum i . Then, as a function of right ascension α , we find the flux density $S_\nu(\alpha)$ that minimizes

$$\chi_S^2(\alpha) = \sum_{ij} [t_i - O_i - S_\nu(\alpha) B_i(\alpha)] V_{ij}^{-1} [t_j - O_j - S_\nu(\alpha) B_j(\alpha)],$$

where $B_i(\alpha)$ is the value of the beam map (single or double difference, as appropriate) centered on observation point i , evaluated at right ascension α . The significance of the fitted flux density is determined by forming the statistic, $F = (\chi_0^2 - \chi_S^2)/(\chi_S^2/N)$, where N is the number of degrees of freedom remaining in the data after fitting out the source. This statistic should be distributed according to an F -distribution with 1 and N degrees of freedom (Martin 1971), which allows us to calculate the cumulative probability $P(F)$ of drawing a value greater than or equal to F if the null hypothesis—that the actual value $S_\nu(\alpha) = 0$ —were true. Values of $F \gg 1$ are highly unlikely under the null hypothesis, and correspond to significant detections of compact features in the data. Figure 1 shows $F(\alpha)$ and $P(F)$ for each of the three frequency bands.

Since we are plotting the cumulative probability of the null hypothesis being true, lower values of $P(F)$ correspond to more significant detections. We have multiple lobe beam patterns, so a bright unresolved feature will alias to several values of right ascension separated by the $40'$ beam throw. Thus, the clusters of peaks near 15^h and 19^h3 do not correspond to multiple features, but rather the aliasing of a single feature into the side beams.

We build a list of candidate unresolved features for each band by iteratively searching for and subtracting the most significant feature, defined here as the maximum value of

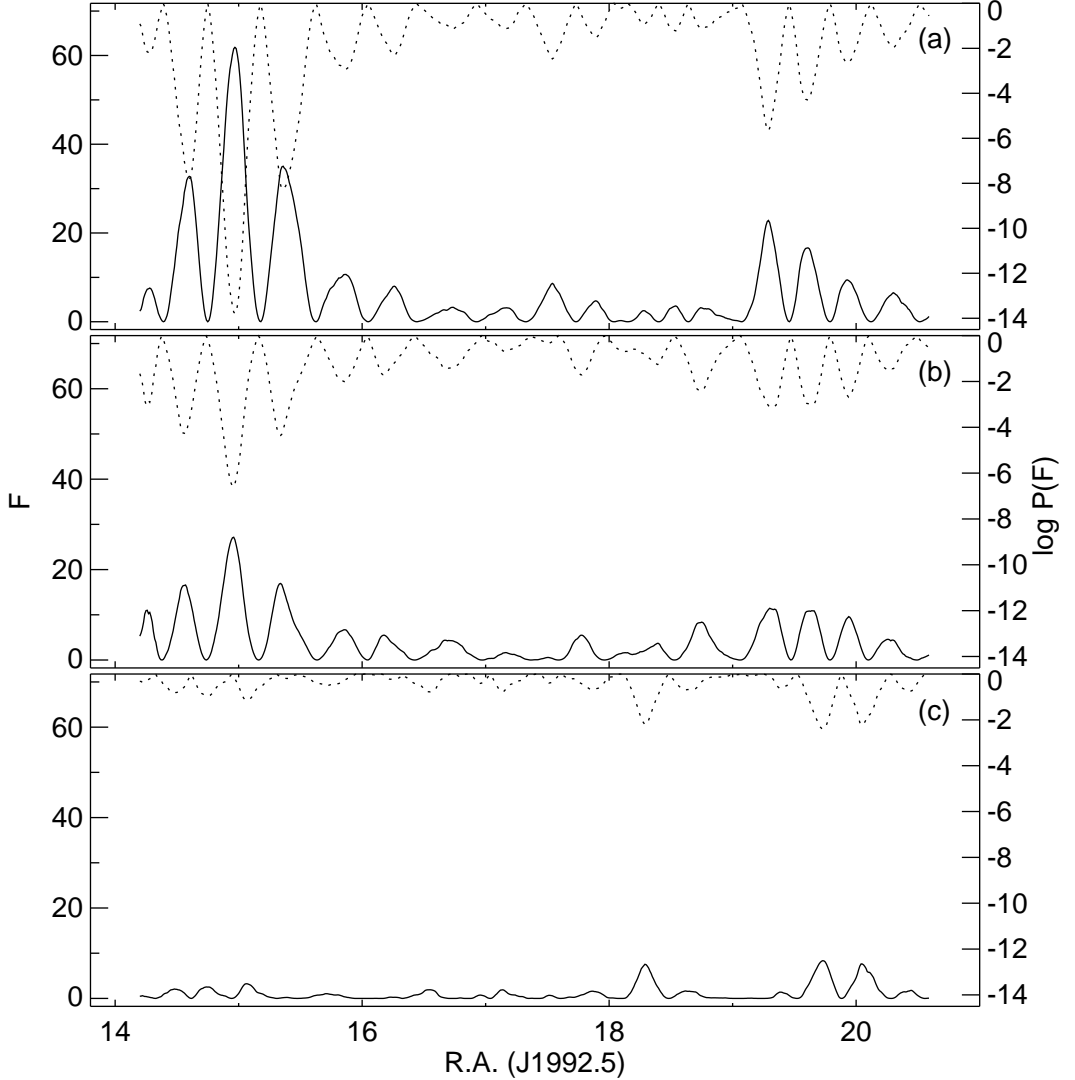


Fig. 1.— F Statistic (solid curve) and cumulative probability $P(F)$ (dotted curve); (a) 5.7 cm^{-1} band, (b) 9.0 cm^{-1} band, (c) 16.5 cm^{-1} band. Low values of $P(F)$ correspond to significant detections. Note that the multi-lobe antenna patterns cause individual sources to alias into several locations (see text).

$F(\alpha)$. After each feature is subtracted, $S_\nu(\alpha)$, and $F(\alpha)$ are re-evaluated to help suppress the aliasing in right ascension. We continue this procedure until $F_{\max} \lesssim 11$, corresponding to $P(F) \geq 10^{-3}$. Three candidate features were identified this way for the 5.7 and 9.3 cm^{-1} bands. We allow each feature to be positive or negative, but the three brightest features are all positive. No features were found at 16.5 cm^{-1} which satisfy the $P(F) < 10^{-3}$ requirement. Table 1 lists the results of this search, along with the corresponding central declinations.

3.3. Spatial Extent

To determine the spatial extent of each feature, we fit the data to a Gaussian shaped surface brightness model, $I_\nu e^{-(\vec{x}-\vec{x}_\alpha)^2/2\sigma^2}$, with the central brightness I_ν , right ascension α , and width $\sigma = \theta_{\text{FWHM}}/(2\sqrt{2 \ln 2})$ as free parameters. The fits are performed using the Levenberg-Marquardt method (Press *et al.* 1992). The total flux density of the feature is related to the central brightness by $S_\nu = 2\pi\sigma^2 I_\nu$.

The fits near 15^h indicate a clearly resolved feature in both the 5.7 and 9.3 cm^{-1} bands, with $\theta_{\text{FWHM}} \approx 35'$. The results of these fits are given in Table 2. There are substantial correlations between θ_{FWHM} and I_ν , so these are also listed. From I_ν , we can also infer an equivalent peak $\Delta T_{\text{CMBR}} = 360 \pm 50 \mu\text{K}$ (5.7 cm^{-1}), $330 \pm 100 \mu\text{K}$ (9.3 cm^{-1}), near 15^h. The fits near 19^h.3 and 19^h.9 do not show evidence for significant spatial extent. We can infer 68% (1- σ) upper bounds on θ_{FWHM} from the estimated parameter variance of the fit; these give $\theta_{\text{FWHM}} < 25'$ at 19^h.3 and $\theta_{\text{FWHM}} < 35'$ at 19^h.9, consistent in both bands.

Because of the close proximity of the 19^h.3 and 19^h.9 features, there is some correlation between their measured flux densities. To account for this, the fits are repeated, omitting θ_{FWHM} while simultaneously fitting for α and S_ν of both features. The results of these fits are shown in Table 3.

3.4. Limits at 16.5 cm^{-1}

While there are no bright features detected at 16.5 cm^{-1} , we can find limits for the corresponding features found at the lower frequencies. For the first feature, we fit using our extended model, fixing $\alpha = 14^{\text{h}}95$ and $\theta_{\text{FWHM}} = 35'$, while for the other features, we fit assuming completely unresolved sources with $\alpha = 19^{\text{h}}31$ and $\alpha = 19^{\text{h}}92$ fixed. In all cases, the results are consistent with zero flux, and upper bounds can be inferred from the variance. These are also listed in Tables 2 and 3

Table 1. Candidate Unresolved Features

R.A. ^a	Dec ^a	<i>F</i>	<i>P(F)</i>	<i>S_ν</i> (Jy)
— Band 1 (5.7 cm ^{−1}) —				
14 ^h 97	+81°97	62	1.6×10^{-14}	+5.5 ± 0.6
19 ^h 29	+81°87	25	6.9×10^{-7}	+2.5 ± 0.5
19 ^h 92	+81°85	14	1.6×10^{-4}	+1.9 ± 0.5
— Band 2 (9.3 cm ^{−1}) —				
14 ^h 96	+81°97	27	2.5×10^{-7}	+4.9 ± 0.9
19 ^h 30	+81°87	12	5.8×10^{-4}	+2.7 ± 0.8
19 ^h 94	+81°85	12	4.9×10^{-4}	+2.9 ± 0.8

^aJ1992.5 coordinates.

Table 2. Fit Results at 15^h

Parameter	Fit Result ^a	Correlations	
		α	θ_{FWHM}
5.7cm ⁻¹	($\chi^2 = 720/627$)		
α :	14 ^h 96±0 ^h 02
θ_{FWHM} :	36'±8'	-0.35	...
$I_{5.7}$:	158±24 kJy/sr	+0.21	-0.68
9.3cm ⁻¹	($\chi^2 = 646/627$)		
α :	14 ^h 95±0 ^h 03
θ_{FWHM} :	33'±13'	-0.32	...
$I_{9.3}$:	137±40 kJy/sr	+0.22	-0.79
16.5cm ⁻¹	($\chi^2 = 542/629$)		
$I_{16.5}$:	-27±77 kJy/sr		

^aErrors are statistical.

Table 3. Fit Results at 19^h3 and 19^h9

Parameter	Fit Result ^a	Correlations		
		$\alpha^{19.3}$	$\alpha^{19.9}$	$S_\nu^{19.3}$
5.7cm ⁻¹ ($\chi^2 = 760/626$)				
$\alpha^{19.3}$:	$19^h 29 \pm 0^h 02$
$\alpha^{19.9}$:	$19^h 92 \pm 0^h 03$	-0.04
$S_{5.7}^{19.3}$:	2.7 ± 0.5 Jy	+0.06	-0.06	...
$S_{5.7}^{19.9}$:	1.9 ± 0.5 Jy	+0.09	+0.02	+0.10
9.3cm ⁻¹ ($\chi^2 = 652/626$)				
$\alpha^{19.3}$:	$19^h 32 \pm 0^h 03$
$\alpha^{19.9}$:	$19^h 93 \pm 0^h 03$	-0.12
$S_{9.3}^{19.3}$:	3.1 ± 0.8 Jy	+0.07	-0.10	...
$S_{9.3}^{19.9}$:	3.0 ± 0.8 Jy	+0.08	+0.06	+0.11
16.5cm ⁻¹ ($\chi^2 = 541/628$)				
$S_{16.5}^{19.3}$:	1.0 ± 2.5 Jy
$S_{16.5}^{19.9}$:	2.9 ± 2.6 Jy	+0.07

^aErrors are statistical.

4. Spectral Models for Features

We now compare the measured spectra of the features with four simple models for astrophysical sources: CMBR anisotropy, free-free emission with $I_\nu \propto \nu^{-0.1}$, synchrotron emission with $I_\nu \propto \nu^{-0.8}$, and cold dust emission with $I_\nu \propto \nu^2 \times (B_\nu(4.8\text{K}) - B_\nu(T_{\text{CMBR}}))$. The last of these is motivated by the possible detection of a cold dust contribution to the Galactic spectrum observed by the *COBE*/FIRAS experiment (Wright *et al.* 1991, Reach *et al.* 1995). Each of the models is fit to the values listed in Tables 2 and 3, the results of which are displayed in Figure 2. The χ^2 for the spectral fits are in Table 4. The relative calibration uncertainty is small compared to the statistical uncertainties, and is not included in the χ^2 values.

All three features are in agreement with the CMBR model. The first two are significantly discrepant with a cold dust spectrum, while the feature near 19^h9 is marginally consistent with that spectrum. Furthermore, this location corresponds to the brightest warm dust emission in our field. Based on this, we cannot rule out the possibility that the 19^h9 feature is due to galactic dust emission.

From these data alone, either free-free or synchrotron emission gives an acceptable fit, and could explain the detections. This would, however, require implausibly large amplitudes for emission at lower frequencies. For example, the best fit free-free spectra, extrapolated to 40 GHz (Q-band), imply antenna temperatures of 3.4, 1.1, and 0.9 mK for the three features; measurements made at Saskatoon of the same field strongly rule out such bright signals (Netterfield *et al.* 1996). The limits on synchrotron emission are even stronger, since the extrapolated temperatures are roughly 3 times greater. Recent measurements of H α emission in this part of the sky imply the free-free contribution to the MSAM1 signal at 5.7cm⁻¹ is <500 Jy/sr rms (Simonetti, Topasna, and Dennison 1996), several orders of magnitude smaller than the signal we report.

5. Searches for Counterparts

5.1. Catalog Searches

We consider the possibility that these detections correspond to compact radio (or infrared) point sources. Note that the power law models corresponding to free-free and synchrotron also can be interpreted as flat-spectrum or steep-spectrum radio spectra, respectively, typical of extragalactic radio sources. No counterparts for the features were found within one beamwidth of the feature locations in the 5 GHz S5 Polar Cap Survey

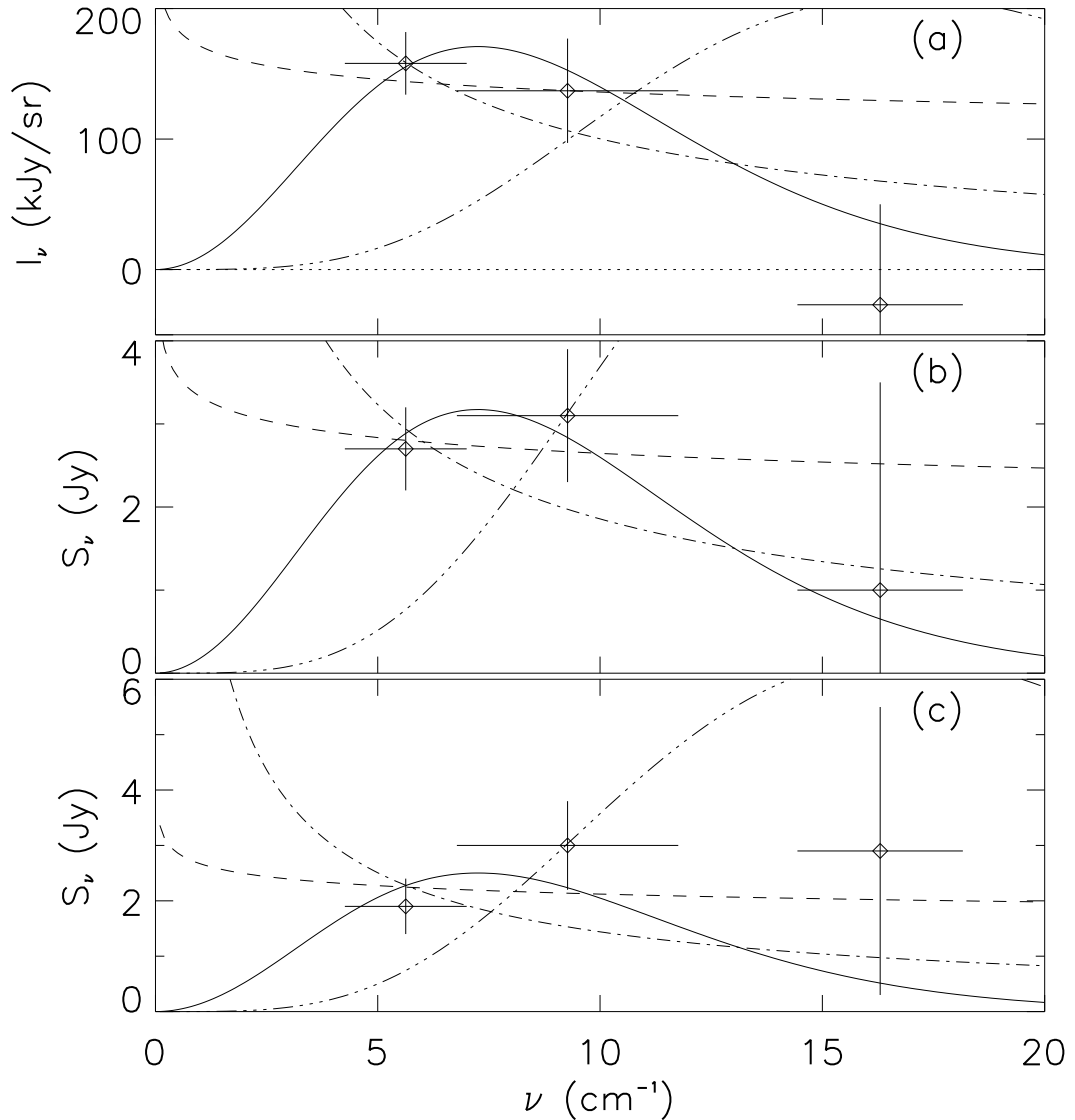


Fig. 2.— Measured spectra for the three features; (a) 14^h95, (b) 19^h3, and (c) 19^h9. Horizontal bars show the effective width of each band. Superimposed are the best fit curves for a CMBR anisotropy spectrum (solid), free-free (dashed), synchrotron emission (dot-dashed), and cold dust (triple-dot-dashed).

Table 4. Spectral Fit χ^2 Values

R.A.	CMBR	Free-Free	Sync	Cold Dust
15 ^h 0	0.8	4.5	2.0	40.
19 ^h 3	0.3	0.7	2.0	20.
19 ^h 9	2.4	1.7	4.3	6.9

Note. — All χ^2 are for 2 degrees of freedom.

(Kühr *et al.* 1981). For all three features, the best-fit flat spectra predict 5 GHz fluxes greater than 3 Jy, while the best-fit steep spectra predict fluxes greater than 40 Jy. The S5 survey is estimated to be complete at 5 GHz down to 250 mJy, providing a strong limit on any flat- or steep-spectrum radio counterpart to the detections.

A similar search was performed with the *IRAS* 100 μm Faint Source Catalog (Moshir *et al.* 1992). A total of 5 objects ranging in flux from 0.9–2.6 Jy were found within one beamwidth of any one of the three features, consistent with the average *IRAS* FSC source density of $\sim 4/\text{sq. degree}$. The contribution of these sources to the MSAM signal is shown to be negligible using the 1.25 mm to 100 μm flux ratio, $(3.1 \pm 0.5) \times 10^{-3}$, determined from a complete sample of *IRAS* galaxies, together with a relatively flat $\nu^{3.2}$ spectrum locally around 1.25 mm (Franceschini and Andreani 1995). The greatest contribution is at 16.5 cm^{-1} , where it is estimated to be ~ 0.1 Jy for each of the latter two features, and ~ 50 mJy for the 15^h feature. The contributions at 9.3 cm^{-1} are a factor of 5 smaller than these, while at 5.7 cm^{-1} they are a factor of 30 smaller. These estimates are reinforced with direct observations at 90 GHz of known *IRAS* sources in the vicinity of the 15^h feature, none of which show significant flux density above the rms noise of 25–50 mJy (Chernin and Scott 1995).

5.2. MSAM1-94

In 1994, we flew the MSAM instrument a second time to observe the same field as the 1992 flight. While the sky overlap between MSAM1-94 and MSAM1-92 was not perfect, it was sufficient to permit an overall comparison of the measurements (Inman *et al.* 1996). We have repeated the fits of §3.3 on the MSAM1-94 data to see if the bright features are present. Near 15^h, there is a corresponding hot spot at $\alpha = 14^{\text{h}}85 \pm 0^{\text{h}}03$ with $\theta_{\text{FWHM}} = 38' \pm 12'$, $I_{5.7} = 106 \pm 32$ kJy/sr, and $I_{9.3} = 71 \pm 62$ kJy/sr (statistical errors only). Near 19^h3 and 19^h9, there are corresponding features that are fit simultaneously as before. At 5.7 cm^{-1} , the resulting parameters are $\alpha = 19^{\text{h}}31 \pm 0^{\text{h}}02$, $S_{5.7}^{19^{\text{h}}3} = 1.3 \pm 0.3$ Jy, and $\alpha = 19^{\text{h}}93 \pm 0^{\text{h}}02$, $S_{5.7}^{19^{\text{h}}9} = 1.4 \pm 0.4$ Jy. At 9.3 cm^{-1} , the fit gives $\alpha = 19^{\text{h}}26 \pm 0^{\text{h}}03$, $S_{9.3}^{19^{\text{h}}3} = 1.8 \pm 0.5$ Jy, and $\alpha = 19^{\text{h}}93 \pm 0^{\text{h}}02$, $S_{9.3}^{19^{\text{h}}9} = 3.2 \pm 0.7$ Jy. The correlations in the MSAM1-94 fits are larger than the MSAM1-92 fits; in particular, the 19^h3 and 19^h9 flux densities have variance correlations of +0.49 at 5.7 cm^{-1} , and +0.42 at 9.3 cm^{-1} . The somewhat smaller flux densities in MSAM1-94 are consistent with the pointing differences between the two flights.

5.3. Other Observations

Since the initial report of these detections in Paper I, a number of groups have searched one or more of these regions for corresponding sources at different wavelengths and/or resolutions. Of particular note is the search reported by Church *et al.* 1995 using the Caltech Submillimeter Observatory on Mauna Kea. This search, which made a deep map of the sky around the 15^h feature at 4.7cm⁻¹ using a 1'7 beam, places an upper limit on any point source in that field of $S_{4.7} < 1$ Jy.

Another observation of this field has recently been reported by Netterfield *et al.* 1996. These observations were made from the ground at Saskatoon, Saskatchewan, Canada, in Q-band (36–46 GHz, 1.2–1.5 cm⁻¹) at 0°.5 resolution, a portion of which were designed to reproduce, as closely as possible, the MSAM observations. A three-lobe beammap, similar to the MSAM double-difference demodulation, was synthesized (the single-difference demodulation is not usable from the ground due to atmospheric noise). Although having somewhat less statistical weight than the MSAM observations, the Saskatoon results correlate well with MSAM, including the bright feature near 15^h right ascension.

6. Simulations

The presence of bright, compact features in the MSAM1-92 data was unexpected. In Paper I, we questioned whether CMBR fluctuations obeying Gaussian statistics could produce such features. To address this issue, we have performed a detailed Monte Carlo simulation of the MSAM observations.

The approach used is similar to that outlined in §4.3 of Paper I¹. We generate numerical realizations of the observations, including contributions from instrument noise and CMBR temperature anisotropies, assuming the anisotropy is a Gaussian random field described by a two-point correlation function, $C(\theta)$. In Paper I, we set limits on the overall amplitude of $\Delta T/T = \sqrt{C(0)}$ by using the likelihood ratio statistic λ ; here, we use those upper and lower bounds to generate realizations which are then searched according to the procedure of §3.2 for unresolved features. Unlike Paper I, here we simulate both demodulations simultaneously, using $\theta_c = 0^{\circ}.4$. We thus determine the distribution of n , the number of unresolved features with $P(F) \leq 10^{-3}$, corresponding to the range of $\Delta T/T$ fluctuations found in the data. Our measured number of sources is $n = 2$ or 3, depending on the

¹Eq (2) in Paper I contains a typographical error, and should read $\langle s_k s_l \rangle = \int d\mathbf{x}_1 d\mathbf{x}_2 H_k(\mathbf{x}_1) H_l(\mathbf{x}_2) C(|\mathbf{x}_1 - \mathbf{x}_2|)$.

assignment of the 19^h9 feature to CMBR or galactic dust. For $\Delta T/T = 1 \times 10^{-5}$, we find the cumulative probability $P(n \geq 2) = 0.20$, $P(n \geq 3) = 0.04$, while for $\Delta T/T = 3 \times 10^{-5}$, $P(n \geq 2) = 0.90$, $P(n \geq 3) = 0.69$. From this, we conclude that bright, compact features such as those observed are in fact consistent with our assumption of Gaussian statistics.

We have also studied the distribution of n using a more physically motivated correlation function, calculated for “standard” flat cold dark matter (CDM) with $\Omega = 1$, $\Omega_B = 0.05$, $\Lambda = 0$, $H_0 = 50\text{km/s/Mpc}$, and no reionization (Sugiyama 1995). Using this model, normalized to the *COBE*/DMR detection $Q_{\text{rms-PS}} = 20\mu\text{K}$ (Górski *et al.* 1994), we find reasonable probabilities for the observed n : $P(n \geq 2) = 0.43$, $P(n \geq 3) = 0.15$. Thus, the detections are consistent with adiabatic fluctuation models such as CDM. Similar results have also been reported for a more generic study of 0°5 resolution CMBR maps (Kogut, Hinshaw, and Bennett 1995).

7. Conclusions

All three features are best described as temperature anisotropies in the CMBR, although the possibility remains that one of these is due to galactic foreground dust emission. While we were initially surprised to find such bright, compact features in the data, we now understand that these are consistent with our assumption of Gaussian fluctuations. Although our catalog searches were all null, we find the most compelling argument that the features are not true point-sources comes from the direct search by Church *et al.* 1995. Finally, the morphological agreement reported by the Saskatoon experiment, consistent with a CMBR anisotropy spectrum spanning three octaves in frequency from Q-band (1.2 cm^{-1}) to the MSAM 9.3 cm^{-1} band, leaves little room for alternate explanations of the detection. Given the agreement with a CMBR temperature anisotropy spectrum, together with the implausibility of other explanations, we conclude that at least the first two, and possibly all three of these detections, are cosmological in origin.

We would like to thank the staff of the National Scientific Balloon Facility (NSBF) for their outstanding support during the two flight campaigns. We would also like to thank E. Magnier, R. Rutledge, C. Bennett, R. Bond, J. Silk, and C. Lawrence for many helpful discussions of these features over the years. This research has made use of NASA’s Astrophysics Data System abstract and article services and IPAC’s XCATSCAN catalog scanning system, as well as software tools from the Free Software Foundation. The National Aeronautics and Space Administration supports this research through grants NAGW 1841, RTOP 188-44, NGT 50908, and NGT 50720.

REFERENCES

Bennett, C. L. *et al.* 1992, *ApJ*, **396**, L7.

Cheng, E. S. *et al.* 1994, *ApJ*, **422**, L37.

Cheng, E. S. *et al.* 1996, *ApJ*, **456**, L71.

Chernin, L. M. and Scott, D. 1995, *Astronomy and Astrophysics*, **296**, 609.

Church, S. E., Mauskopf, P. D., Ade, P. A. R., Devlin, M. J., Holzapfel, W. L., Wilbanks, T. M., and Lange, A. E. 1995, *ApJ*, **440**, L33.

Donat III, W. and Boksenberg, A., editors 1993. *The Astronomical Almanac for the year 1994*. U.S. Government Printing Office and HMSO, Washington, D.C. and London.

Fixsen, D. J. *et al.* 1996, *ApJ*. submitted, preprint [astro-ph/9512006](#).

Franceschini, A. and Andreani, P. 1995, *ApJ*, **440**, L5.

Górski, K. M. *et al.* 1994, *ApJ*, **430**, L89.

Griffin, M. J., Ade, P. A. R., Orton, G. S., Robson, E. I., Gear, W. K., Nolt, I. G., and Radostitz, J. V. 1986, *Icarus*, **65**, 244.

Hagen, J. B. and Boksenberg, A., editors 1991. *The Astronomical Almanac for the year 1992*. U.S. Government Printing Office and HMSO, Washington, D.C. and London.

Inman, C. A. *et al.* 1996, *ApJ*. submitted, preprint [astro-ph/9603017](#).

Kogut, A., Hinshaw, G., and Bennett, C. L. 1995, *ApJ*, **441**, L5.

Kühr *et al.* 1981, *AJ*, **86**, 854.

Martin, B. R. 1971. *Statistics for Physicists*. Academic, London.

Moshir, M. *et al.* 1992. *IRAS Faint Source Survey: Explanatory Supplement*. JPL D-10015 8/92. JPL, Pasadena, CA., second edition.

Netterfield, C. B., Devlin, M. J., Jarosik, N., Page, L., and Wollack, E. J. 1996, *ApJ*. submitted, preprint [astro-ph/9601197](#).

Press, W. H., Teukolsky, S. A., Vetterling, W. T., and Flannery, B. P. 1992. *Numerical Recipes in FORTRAN: The Art of Scientific Computing*. Cambridge University Press, Cambridge, 2nd edition.

Reach, W. *et al.* 1995, *ApJ*, **451**, 188.

Simonetti, J. H., Topasna, G. A., and Dennison, B. 1996, *BAAS*. submitted.

Sugiyama, N. 1995, *ApJS*, **100**, 281.

Weiss, R. 1980, *ARA&A*, **18**, 489.

White, M., Scott, D., and Silk, J. 1994, *ARA&A*, **32**, 319.

Wright, E. L. *et al.* 1991, *ApJ*, **381**, 200.